



Intense Geomagnetically Induced Currents (GICs): Association with Solar and Geomagnetic Activities

Rajkumar Hajra¹

Received: 29 October 2021 / Accepted: 22 December 2021
© The Author(s), under exclusive licence to Springer Nature B.V. 2022

Abstract

We present a statistical study of the intense geomagnetically induced currents (GICs) in the subauroral region, which can damage ground electronic systems. From the natural gas pipeline recordings taken near Mäntsälä, Finland (geographic: 60.6°N, 25.2°E), 605 GICs with peak intensity > 10 A were registered from 1999 through 2019, ≈ 2 solar cycles. During Solar Cycle 23, the occurrence peak was observed during the solar maximum with fewer events during the descending phase and no events during the solar minimum. Overall a lower occurrence rate was recorded during Solar Cycle 24. There was an asymmetric semi-annual variation of events with a larger number during September–November than during March–April, and the lowest occurrence around the Summer solstice. While only one event was recorded during geomagnetic quiet conditions ($\text{SYM-H} > -50$ nT), $\approx 2\%$ of all events were associated with moderate (-50 nT $> \text{SYM-H} \geq -100$ nT), $\approx 31\%$ with intense (-100 nT $> \text{SYM-H} \geq -250$ nT), and $\approx 67\%$ with superintense ($\text{SYM-H} < -250$ nT) geomagnetic storms. Among these, $\approx 72\%$ occurred in the storm main phase and $\approx 28\%$ in the recovery phase. Interplanetary sheaths are found to be the most efficient events causing the majority ($\approx 50.8\%$) of the GICs with peak intensity > 10 A followed by magnetic clouds ($\approx 44.0\%$), corotating interaction regions ($\approx 3.1\%$), fast forward shocks following the sheaths ($\approx 1.9\%$), and solar wind high-speed streams ($\approx 0.2\%$).

Keywords Coronal mass ejections, interplanetary · Magnetic fields, interplanetary · Magnetosphere, geomagnetic disturbances · Solar cycle · Solar wind

1. Introduction

Geomagnetically induced currents (GICs; Barlow, Barlow, and Culley, 1849; Varley, 1873; Campbell, 1980; Akasofu and Aspnes, 1982) are known to be a ground manifestation of space weather events that initiate on the Sun (see Gaunt, 2016; Lakhina, Hajra, and Tsutsumi, 2021, for reviews on the topic). Solar coronal mass ejections (CMEs), solar wind high-speed ($\approx 550\text{--}800$ km s⁻¹) streams (HSSs) emanated from coronal holes, and corotating interaction regions (CIRs) between HSSs and the slow wind lead to geomagnetic

✉ R. Hajra
rajkumarhajra@yahoo.co.in

¹ Indian Institute of Technology Indore, Simrol, Indore, 453552, India

disturbances through the process of the solar wind–magnetosphere coupling (Dungey, 1961; Gonzalez et al., 1994). The consequent rapid geomagnetic field changes ($dB/dt > 1 \text{ nT s}^{-1}$) result in low-frequency ($\approx 0.001 - 1 \text{ Hz}$) GICs. The currents flow through ground electronic systems, namely electric power transmission grids, oil and gas pipelines, phone cables, and railway systems, which can be damaged in the case of extreme GIC flows. There are a few examples of reported hazardous effects of GICs during extreme space weather events: (1) the Carrington storm of September 1859 causing disruptions of the telegraph operations in North America (Loomis, 1861); (2) the March 1989 storm causing the collapse of the Hydro-Québec power system in Canada (Allen et al., 1989); (3) the Halloween storm of October 2003 causing a large-scale transformer collapse near Malmö, Sweden (Pulkkinen et al., 2005). In fact, due to the growing dependence of modern society on electronic technology, such GIC hazards have significant socio-economic implications (e.g. Oughton et al., 2017), particularly in high-latitude regions.

Thus, it is important to know the occurrence probability of intense GIC events and understand the underlying geomagnetic and solar/interplanetary processes. The subauroral zone GIC occurrence is known to be centered around local midnight (Viljanen et al., 2001, 2006; Hajra, 2022) due to its association with auroral activity (Barlow, Barlow, and Culley, 1849; Campbell, 1980; Akasofu and Aspin, 1982). Huttunen et al. (2008) studied the Mäntsälä, Finland (geomagnetic latitude: 57.9°N , geographic latitude: 60.6°N , geographic longitude: 25.2°E) GIC events $> 10 \text{ A}$, which are rare, and considered them to be “extreme” at this location (Pulkkinen et al., 2001) during Solar Cycle 23 (1999–2005). It was shown that the number of days with GICs $> 10 \text{ A}$ was the highest during the solar maximum years and also during the descending phase. Interplanetary sheaths, a part of the interplanetary coronal mass ejections (ICMEs), were suggested to be the most important solar driver of the large GICs. More recently, Tsurutani and Hajra (2021) reported the association of the majority of the extreme GICs at Mäntsälä with the October 2003 Halloween superstorm and suggested the importance of extremely intense substorms (Tsurutani et al., 2015; Hajra et al., 2016; Hajra and Tsurutani, 2018) in causing extreme GICs. We aim to extend the Huttunen et al. (2008) work using a longer database (as used by Tsurutani and Hajra, 2021) for a better understanding of extreme GIC events as well as their seasonal, solar cycle, geomagnetic, and solar event dependencies.

In this article, we will identify all intense GIC events with peak intensity $> 10 \text{ A}$ occurring at Mäntsälä between 1999 and 2019, ≈ 2 solar cycle period. Using the 21-year-long GIC database, we will study the seasonal and solar cycle dependencies of the events. We will also study the dependence on geomagnetic storm intensity and phase. In addition, the efficiency of different space weather events in causing extreme GICs will be explored. Such a study is important in order to understand the event occurrence probability and associated risks, as well as to develop predictive models based on solar and geomagnetic observations.

2. Data Analyses and Results

2.1. Intense GICs During 7–8 November 2004: A Case Study Based on Associated Solar and Geomagnetic Activity

Figure 1 shows an example of intense GIC events at Mäntsälä and associated geomagnetic and solar/interplanetary conditions during 7–8 November 2004. The GIC data are collected from the Space and Earth Observation Centre of the Finnish Meteorological Institute (<https://space.fmi.fi/gic/index.php>; Viljanen and Pirjola, 1989; Pulkkinen et al., 2001;

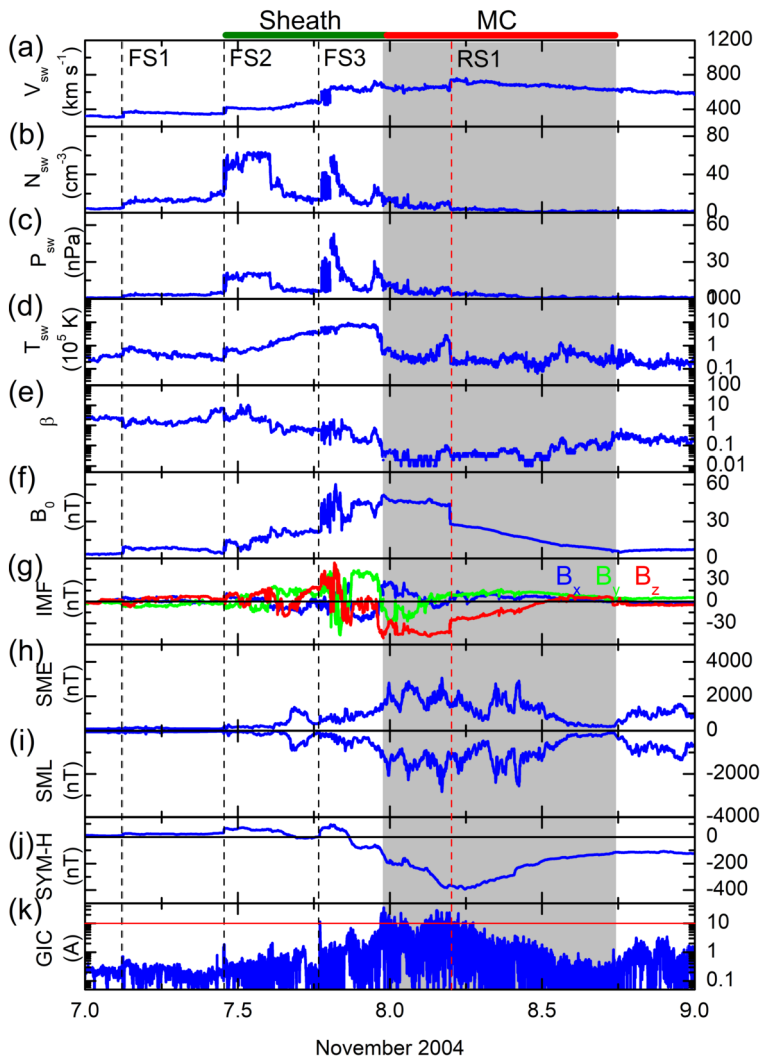


Figure 1 Intense GIC events and associated geomagnetic and solar/interplanetary events during 7–8 November 2004. From top to bottom, panels show the variations of (a) the solar wind plasma speed V_{sw} , (b) the plasma density N_{sw} , (c) the ram pressure P_{sw} , (d) the plasma temperature T_{sw} , (e) the plasma β , (f) the IMF magnitude B_0 , (g) the IMF components B_x , B_y , and B_z in the same panel, (h) the SME index, (i) the SML index, (j) the SYM-H index, and (k) the absolute values of GICs at Mäntsälä. The red horizontal line in the GIC panel indicates $GIC = 10$ A level. The black vertical dashed lines indicate three fast forward shocks FS1, FS2, and FS3. The red vertical dashed line indicates a fast reverse shock RS1. An interplanetary sheath interval is marked by a horizontal green bar at the top. A magnetic cloud (MC) is marked by a shaded region and a horizontal red bar at the top.

Viljanen et al., 2010). The GIC data have a resolution of 10 seconds, and the measurement noise level is ≈ 0.1 A (Viljanen et al., 2006). While GICs can be both positive and negative, the absolute values of GICs are analyzed in this work (Figure 1k). During the interval from $\approx 18:29$ UT on 7 November to $\approx 11:28$ UT on 8 November, a total of 38 GICs with peaks > 10 A (GIC_p) were recorded. GIC_p varied between ≈ 10.3 A and ≈ 35.4 A. The GIC

peaks had a duration between ≈ 1.2 and ≈ 8.0 minutes, with an average (median) duration of ≈ 3.6 minutes (≈ 3.3 minutes) for all peaks.

The auroral substorm activity during the above interval is studied using the auroral ionospheric SuperMAG AE (SME) (Figure 1h) and SuperMAG AL (SML) (Figure 1i) indices. They represent the eastward and westward auroral electrojet currents, respectively, flowing at ≈ 100 km altitude (Davis and Sugiura, 1966). These 1 minute indices are based on ≈ 300 ground-based magnetometer measurements of the geomagnetic fields (horizontal) under the worldwide SuperMAG network (<http://supermag.jhuapl.edu/>; Gjerloev, 2009; Newell and Gjerloev, 2011). There is a strong association between intense GICs (Figure 1k) and intense auroral activity (Figure 1h–i). Both SME and SML are found to be enhanced from $\approx 14:38$ UT on 7 November to $\approx 15:37$ UT on 8 November with their peak values of 3060 nT and -2864 nT, respectively.

The geomagnetic storm activity during the above interval is studied by the symmetric ring current index (SYM-H) variation (Figure 1j). The SYM-H index (Wanliss and Showalter, 2006; Iyemori et al., 2010) represents the geomagnetic field depressions due to the storm time ring current particle enhancement at $\approx 2-7$ Earth radii from the Earth in its equatorial plane (Frank, 1967; Shelley, Johnson, and Sharp, 1972; Williams, 1987; Hamilton et al., 1988; Daglis et al., 1999). The 1 minute SYM-H data are obtained from the World Data Center for Geomagnetism, Kyoto, Japan (<http://wdc.kugi.kyoto-u.ac.jp/>). From the SYM-H variation, a superintense ($\text{SYM-H} \leq -250$ nT) geomagnetic storm (Gonzalez et al., 1994) can be identified that started at $\approx 19:20$ UT on 7 November and reached a peak intensity of -394 nT at $\approx 05:47$ UT on 8 November, marking the end of the main phase and/or starting of the storm recovery phase. Most (36) of the GIC > 10 A peaks are found to occur during the main phase of the storm and only 2 in the recovery phase.

The solar wind/interplanetary conditions are explored using the solar wind plasma and interplanetary magnetic field (IMF) measurements shifted to the Earth's bow shock nose. The 1 minute data are collected from NASA's OMNIWeb (<https://omniweb.gsfc.nasa.gov/>). The IMFs are shown in the geocentric-solar-magnetospheric (GSM) coordinate system, where the x -axis is directed from the Earth to the Sun, the y -axis is perpendicular to the Earth's magnetic dipole so that the $x-z$ plane contains the dipole axis. The positive z -axis is chosen to be in the same sense as the northern magnetic pole.

From simultaneous and sharp increases in the solar wind speed V_{sw} (Figure 1a), plasma density N_{sw} (Figure 1b), ram pressure P_{sw} (Figure 1c), temperature T_{sw} (Figure 1d), and IMF magnitude B_0 (Figure 1f), three interplanetary fast forward shocks (FSs) are identified at $\approx 03:00$ UT (FS1), $\approx 11:00$ UT (FS2), and $\approx 18:32$ UT (FS3) on 7 November. These are shown by black vertical dashed lines. A fast reverse shock (RS1) is observed at $\approx 04:43$ UT on 8 November as identified from the sharp increase in V_{sw} and simultaneous decreases in N_{sw} , P_{sw} , T_{sw} , and B_0 (red vertical dashed line). The shocks are caused by CMEs moving in the interplanetary medium (that is, ICMEs) faster than the local magnetosonic speed (V_{ms}) (Tsurutani et al., 2011; Hajra, 2021a). The FSs propagate in the same direction of their driving ICMEs, while the RSs propagate in the opposite direction. In both cases, however, the shock propagation speeds are less than the ambient V_{sw} , and thus both FSs and RSs are convected by the solar wind in the antisunward direction. An ICME-driven FS is followed by an interplanetary sheath characterized by a compressed, heated, and turbulent solar wind plasma and large-amplitude IMF variations (Kennel, Edmiston, and Hada, 1985; Tsurutani et al., 1988). Thus, in the plasma rest frame, N_{sw} , T_{sw} , and B_0 increase in the sheath downstream of the FS. On the other hand, in the case of a sunward propagating RS, the sunward side is the upstream unshocked region. Therefore, N_{sw} , T_{sw} , and B_0 decrease in the sheath following an RS. The fast FS1, FS2, and FS3 caused sudden impulses (SI^+) in SYM-H

of +19, +50, +61 nT (Figure 1j), respectively, and impulsive GICs of ≈ 0.7 , ≈ 1.9 , and ≈ 11.4 A (Figure 1k), respectively.

Following the shock FS2, the interval up to $\approx 23:28$ UT on 7 November is characterized by strongly fluctuating plasma and IMF components. This is identified as an interplanetary sheath (green horizontal bar at the top). Short episodes of southward IMFs inside the sheath caused small increases (decreases) in SME (SML) and initiation of the geomagnetic storm, as can be noted in the first-step decreasing trend in SYM-H during the three-step geomagnetic storm main phase. During this sheath interval, a total of 3 GIC > 10 A peaks are recorded (Figure 1k).

The sheath is followed by an enhanced IMF B_0 of ≈ 46 nT (Figure 1f), smooth rotations in the IMF components (Figure 1g), a low T_{sw} of $\approx 0.08 \times 10^5$ K (Figure 1d), and a low plasma β of ≈ 0.02 (Figure 1e) up to $\approx 18:00$ UT on 8 November. This represents a flux rope magnetic cloud (MC), which is known to be an important part of a significant fraction of ICMEs impinging on the Earth (Burlaga et al., 1981; Klein and Burlaga, 1982; Tsurutani and Gonzalez, 1997). The MC is shown by the shaded region and a red horizontal bar at the top. The strong (-50 nT) and long-duration (≈ 13 h) southward IMF component of the MC caused the major part of the geomagnetic storm main phase (Figure 1j) and major substorm activity (Figure 1h–i). The MC was associated with 35 GIC > 10 A peaks (Figure 1k).

During the entire period of this study, from 1999 through 2019, we identified a total of 605 GIC > 10 A peaks (GIC_p) at Mäntsälä. For each of the peaks, we identified their month and year of occurrence, and their association with the geomagnetic storm intensity and phase, as well as the associated solar/interplanetary events. The statistical analysis of this large database is presented in the following sections.

2.2. Seasonal and Solar Cycle Dependencies

The 605 $GIC_p > 10$ A detected at Mäntsälä are found to have a wide range of intensity, from > 10 A to ≈ 60 A. Figure 2c shows the year-month contour plot of GIC_p during each month and year of observation using a color coding. The GIC_p values corresponding to each color are shown by the color bar at the right. The GIC_p numbers in each month of observation are shown by embedded numbers inside the contour plot. About 66% of the events are found to have GIC_p in the range of 10–15 A, and the number of events decreases with increasing GIC_p (Figure 2d).

To study the solar cycle dependence of the intense GIC events, we estimated the number of GIC peaks and mean values of their intensity in each year. Similarly, we estimated the monthly numbers and monthly means of GIC peaks in order to study their seasonal dependence.

Solar cycle dependence of GIC_p is shown by the histograms of the yearly numbers (gray) and the yearly means (empty) of the peaks in each year of observation (Figure 2b). The yearly mean $F_{10.7}$ solar flux is superposed to show the ≈ 11 -year solar cycle phases (Schwabe, 1844). This is obtained from the Laboratory for Atmospheric and Space Physics (LASP) Interactive Solar Irradiance Data Center (<https://lasp.colorado.edu/lisird/>). Apparently, a larger number of events was recorded during Solar Cycle 23 (1999–2008) than during Cycle 24 (2009–2019). This result seems to be consistent with the fact that among all cycles in the space age (from 1957 on), Solar Cycle 24 is the weakest one in solar activity, solar wind-magnetosphere coupling, and geomagnetic activity (see Hajra, 2021b; Hajra et al., 2021, for a detailed discussion). However, it should be noted that there are more gaps in observation around Solar Cycle 24 maximum. Thus, any difference between solar cycles requires further investigation. In Solar Cycle 23, most of the intense GIC_p are centered

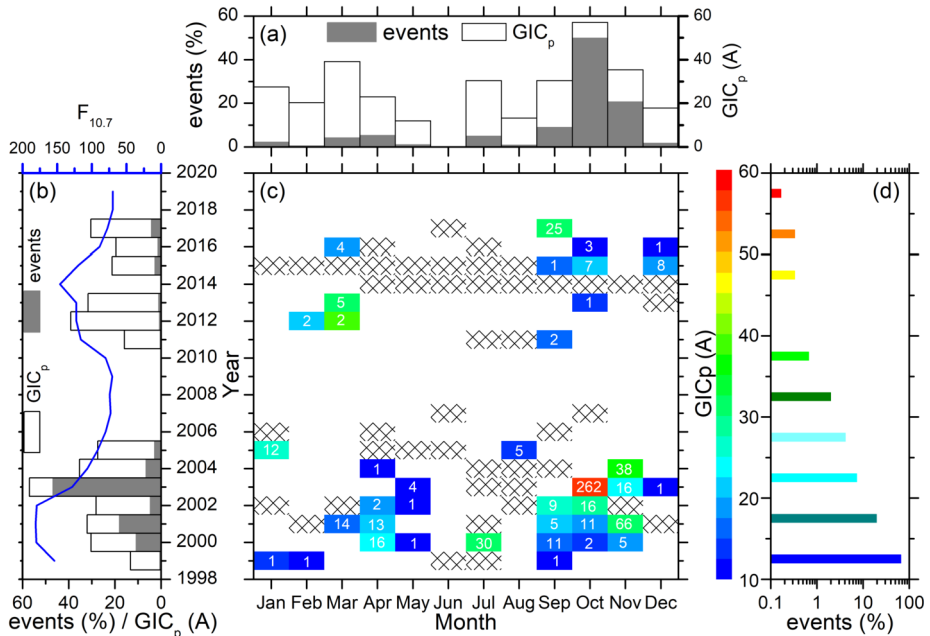


Figure 2 Solar cycle and seasonal distributions of the GIC > 10 A events. **(a)** The monthly occurrence frequency (gray bars, scale on the left) and the monthly peak intensities (empty bars, scale on the right) of the GIC events. **(b)** The yearly occurrence frequency (gray bars) and the yearly peak intensities (empty bars) of the GIC events (scales at the bottom), and the yearly mean $F_{10.7}$ solar flux variations (blue curve, scale on the top). **(c)** The year-month contour plot showing the distributions of the monthly peak intensities of the GIC > 10 A events during the entire period of observation. The GIC intensities given by different colors are shown by the bar on the right. Numbers inside the contour plot correspond to the event numbers in each month and year. The data gaps are shown by crosses. **(d)** Distribution of the events with varying GIC intensity.

around the solar cycle maximum, followed by a decreasing number and intensity with decreasing $F_{10.7}$ solar flux. No such intense events were recorded during the solar minima, 2006–2010 and 2018–2019. Overall, a correlation of the GIC_p with the yearly mean $F_{10.7}$ solar flux is prominent. This will be discussed again in this article.

In Solar Cycle 23, events are found to occur around equinoxes (April–May and September–October) (Figure 2c). However, no such seasonal dependence can be inferred for Solar Cycle 24. Thus, no clear overall seasonal variation is prominent in the GIC_p occurrence in Figure 2a, except the largest occurrence frequency in October. However, the October peak is mainly given by 262 events in 2003 (Tsurutani and Hajra, 2021). The events seem to be more intense during February–April and September–November than during May–July (Figure 2a). As the subauroral zone GIC events are strongly associated with auroral substorms (e.g. Barlow, Barlow, and Culley, 1849; Campbell, 1980; Akasofu and Aspnes, 1982; Viljanen et al., 2001, 2006; Hajra, 2022), the GIC seasonal dependence is found to be consistent with the seasonal variations of substorms (see Wang and Lüher, 2007; Mursula, Tanskanen, and Love, 2011; Tanskanen et al., 2011; Marques de Souza Franco et al., 2021, and references therein). Several processes, such as the solar hemispheric asymmetry, variations in the solar wind-magnetosphere-ionosphere coupling, the ionospheric conductivity, are suggested as the possible factors controlling the seasonal variation. The present result may indicate the important role of the substorm-related precipitation that can

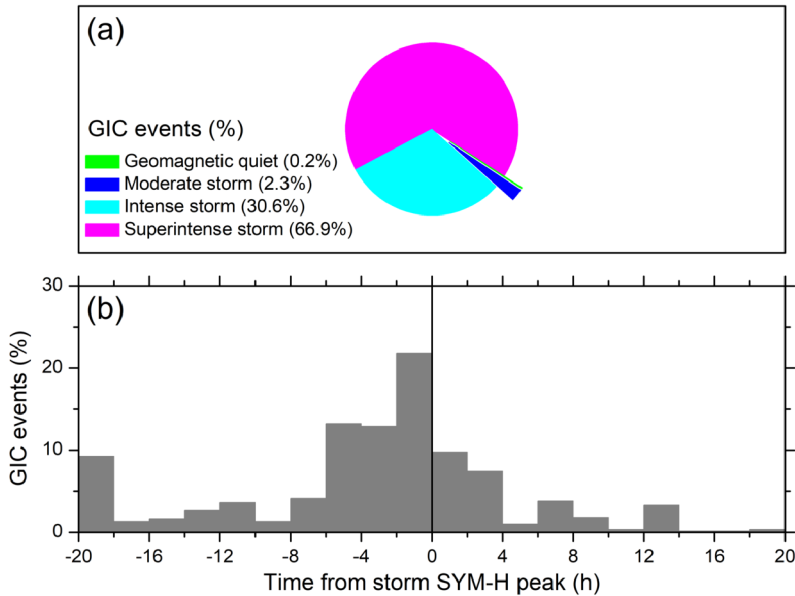


Figure 3 Geomagnetic storm dependence of the GIC > 10 A events. **(a)** Pie chart showing the percentage occurrence of the GIC > 10 A events under different geomagnetic conditions. **(b)** Distribution of the GIC > 10 A events in the time before or after the magnetic storm SYM-H peak intensity ($t = 0$) in histogram format.

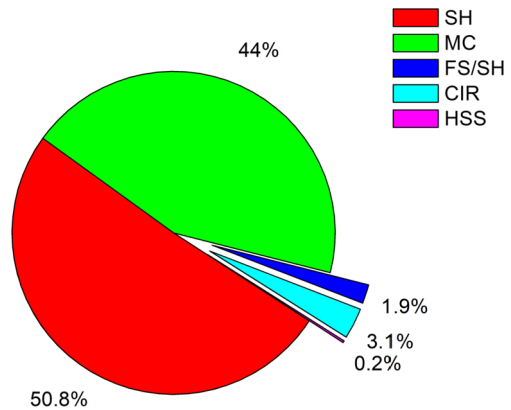
enhance the ionospheric conductivity and can induce the generation of intense GIC events. However, significant observational gaps may have some modulation in the observed seasonal variation.

2.3. Geomagnetic Storm Dependence

Among 605 GIC_p > 10 A events detected during the 1999–2019 period, only one occurred during geomagnetic quiet conditions (SYM-H > -50 nT). The rest of them were associated with geomagnetic storms of varying intensity. A geomagnetic storm is identified by this criterion (Gonzalez et al., 1994): SYM-H minimum < -50 nT. Based on the SYM-H minimum values, geomagnetic storms are classified as: moderate (-50 nT > SYM-H ≥ -100 nT), intense (-100 nT > SYM-H ≥ -250 nT), and superintense (SYM-H < -250 nT). The GIC_p > 10 A distribution under different geomagnetic conditions is shown by the pie chart in Figure 3a. About 2% of all events were associated with moderate magnetic storms, ≈ 31% with intense, and ≈ 67% with superstorms. This indicates that the stronger the magnetic storm, the higher is the probability of intense GIC occurrence.

The histogram in Figure 3b shows the distribution of GIC events with respect to the magnetic storm SYM-H peak occurrence ($t = 0$ h). The events on the left side of $t = 0$ occurred during the magnetic storm main phase, and those on the right side of $t = 0$ correspond to the storm recovery phase. About 72% of all GIC_p > 10 A occurred in the storm main phase, and only 28% in the recovery phase. Interestingly, ≈ 48% of the events took place in the time interval between 6 h prior to and the SYM-H peak time.

Figure 4 Pie chart showing the percentage of the GIC > 10 A events caused by interplanetary sheaths (SHs), magnetic clouds (MCs), fast forward shocks followed by sheaths (FS/SHs), corotating interaction regions (CIRs), and solar wind high-speed streams (HSSs).



2.4. Solar/Interplanetary Event Dependence

We identified the interplanetary structures associated with each of the GIC > 10 A peaks (Figure 4). An interplanetary fast FS is identified by the sharp and simultaneous increases in the solar wind V_{sw} , N_{sw} , P_{sw} , T_{sw} , and IMF B_0 (Tsurutani et al., 2011). An interplanetary sheath is identified by fluctuating N_{sw} and IMF following an FS (Kennel, Edmiston, and Hada, 1985; Tsurutani et al., 1988). An MC is identified by the enhanced B_0 , smooth rotation(s) in the IMF component(s), low T_{sw} and β (Burlaga et al., 1981; Klein and Burlaga, 1982; Tsurutani and Gonzalez, 1997). A solar wind HSS is identified by the V_{sw} peak in the range of ≈ 550 – 800 km s $^{-1}$. To confirm its solar origin as a coronal hole, we verified solar images taken by the Atmospheric Imaging Assembly (AIA) telescope of NASA's Solar Dynamics Observatory (SDO; <https://sdo.gsfc.nasa.gov/>). A CIR is identified by the compressed (high) N_{sw} , P_{sw} , and B_0 in the interaction region between a slow (≈ 300 – 400 km s $^{-1}$) stream and an HSS (Belcher and Davis, 1971; Siscoe, 1972; Krieger, Timothy, and Roelof, 1973; Smith and Wolfe, 1976; Pizzo, 1978).

Among the 605 GIC_p events, only one occurred during the solar wind HSS. Only $\approx 3\%$ of the events occurred during CIRs. An overwhelming majority ($\approx 97\%$) of events were associated with ICMEs. More specifically, $\approx 51\%$ occurred during the interplanetary sheath and $\approx 44\%$ during the MC portion of an ICME.

3. Discussion

We identified 605 GIC > 10 A peaks during a 21-year period, from 1999 to 2019, from the natural gas pipeline recordings at Mäntsälä, Finland, located in the subauroral region. The ≈ 2 solar-cycle-long GIC observation, characterized by varying solar activity, geomagnetic activity, and space weather events, is suitable to identify broad variability patterns of the GICs. The major results are discussed below.

Dependence of the intense GICs on the geomagnetic storm phase and strength is reported for the first time. It was shown by Tsurutani and Hajra (2021) that $\approx 43\%$ of all GIC > 10 A, and $\approx 43\%$ of all GIC > 30 A peaks (during 1999–2019) occurred during the two Halloween superstorms of 29–31 October 2003. For the first time, our study shows the statistical significance of this finding. Storms with increasing strength, from moderate to superintense, are found to be associated with a linearly increasing number of GIC > 10 A

peaks. About 67% of all GIC > 10 A peaks were associated with superstorms. This result is expected, as stronger geomagnetic storms can induce stronger variations in geomagnetic fields resulting in an intense GIC activity. Interestingly, an overwhelming majority ($\approx 72\%$) of the peaks occurred during the storm main phase, when the geomagnetic field fluctuation is larger than that in the storm recovery phase. A similar magnetic storm phase dependence was reported for the extremely intense substorms or supersubstorms (SSSs) with the SML peak intensity (minimum) < -2500 nT (Hajra et al., 2016). Such a storm dependence of GICs is reported for the first time.

Among the space weather events, ICMEs are found to cause $\approx 97\%$ of the GIC > 10 A peaks. Sheath and MC portions of the ICME are found to be associated with $\approx 51\%$ and $\approx 44\%$ of all peaks, respectively. As mentioned before, ICMEs (in particular, interplanetary sheaths) represent turbulent solar wind plasma and IMF. Associated large-amplitude plasma and magnetic field fluctuations are conducive to geomagnetic field fluctuations. The above results are consistent with Huttunen et al. (2008) reporting ICMEs to be associated with 91% of the days with GIC > 10 A peaks during Solar Cycle 23. However, it should be noted that the Huttunen et al. (2008) statistics is based on the days with the GIC > 10 A peaks, while the present work considers the individual peaks. It should be noted as well that, a particular day may be associated with several GIC > 10 A peaks, and that the same day can be characterized by more than one interplanetary structure. Thus, the present work exploring the association of the individual peaks with interplanetary structures is much more robust and accurate.

The strong association of intense GICs with superstorms and ICMEs can explain the GIC occurrences during Solar Cycle 23 maximum. ICMEs are known to be major drivers of superstorms (Echer, Gonzalez, and Tsurutani, 2008), and superstorms exhibit a maximum during solar maximum (e.g., Hajra et al., 2021; Temmer, 2021, and references therein). Thus, it is expected that intense GICs which are found to be associated with superstorms and ICMEs (present work) exhibit a similar solar cycle dependence.

In conclusion, robust statistics of subauroral zone, intense GICs is presented. Strong associations of intense GICs with intense storms, particularly in their main phase, and with ICMEs can have important implications for developing predictive models of GICs and associated risks. Space-based monitoring of space weather events and ground-based monitoring of geomagnetic activity can be utilized to predict GICs.

Acknowledgments The work is funded by the Science and Engineering Research Board (SERB, grant no. SB/S2/RJN-080/2018), a statutory body of the Department of Science and Technology (DST), Government of India through the Ramanujan Fellowship.

Author Contribution I am the sole author of this paper.

Data Availability The Mäntsälä GIC data are available at the Space and Earth Observation Centre of the Finnish Meteorological Institute (<https://space.fmi.fi/gic/index.php>). The auroral SME and SML indices are available at the SuperMAG site (<http://supermag.jhuapl.edu/>). The geomagnetic SYM-H index data are available at the World Data Center for Geomagnetism, Kyoto, Japan (<http://wdc.kugi.kyoto-u.ac.jp/>). The solar wind plasma and IMF data are available at NASA's OMNIWeb (<https://omniweb.gsfc.nasa.gov/>). The solar images are available at NASA's Solar Dynamics Observatory (SDO; <https://sdo.gsfc.nasa.gov/>). The $F_{10.7}$ solar flux data are available at the Laboratory for Atmospheric and Space Physics (LASP) Interactive Solar Irradiance Data Center (<https://lasp.colorado.edu/lisird/>).

Declarations

Conflict of Interest I declare no conflict of interests.

References

- Akasofu, S.-I., Aspnes, J.D.: 1982, Auroral effects on power transmission line systems. *Nature* **295**, 136. DOI.
- Allen, J., Sauer, H., Frank, L., Reiff, P.: 1989, Effects of the March 1989 solar activity. *Eos Trans. AGU* **70**, 1479. DOI.
- Barlow, W.H., Barlow, P., Culley, R.S.: 1849, VI. On the spontaneous electrical currents observed in the wires of the electric telegraph. *Phil. Trans. Roy. Soc. London* **139**, 61. DOI.
- Belcher, J.W., Davis, L. Jr.: 1971, Large-amplitude Alfvén waves in the interplanetary medium, 2. *J. Geophys. Res.* **76**, 3534. DOI.
- Burlaga, L., Sittler, E., Mariani, F., Schwenn, R.: 1981, Magnetic loop behind an interplanetary shock: Voyager, Helios, and IMP 8 observations. *J. Geophys. Res.* **86**, 6673. DOI.
- Campbell, W.H.: 1980, Observation of electric currents in the Alaska oil pipeline resulting from auroral electrojet current sources. *Geophys. J. Int.* **61**, 437. DOI.
- Daglis, I.A., Thorne, R.M., Baumjohann, W., Orsini, S.: 1999, The terrestrial ring current: Origin, formation, and decay. *Rev. Geophys.* **37**, 407. DOI.
- Davis, T.N., Sugiura, M.: 1966, Auroral electrojet activity index AE and its universal time variations. *J. Geophys. Res.* **71**, 785. DOI.
- Dungey, J.W.: 1961, Interplanetary magnetic field and the auroral zones. *Phys. Rev. Lett.* **6**, 47. DOI.
- Echer, E., Gonzalez, W.D., Tsurutani, B.T.: 2008, Interplanetary conditions leading to superintense geomagnetic storms ($Dst \leq -250$ nT) during solar cycle 23. *Geophys. Res. Lett.* **35**, L06S03. DOI.
- Frank, L.A.: 1967, On the extraterrestrial ring current during geomagnetic storms. *J. Geophys. Res.* **72**, 3753. DOI.
- Gaunt, C.T.: 2016, Why space weather is relevant to electrical power systems. *Space Weather* **14**, 2. DOI.
- Gjerloev, J.W.: 2009, A global ground-based magnetometer initiative. *Eos Trans. AGU* **90**, 230. DOI.
- Gonzalez, W.D., Joselyn, J.A., Kamide, Y., Kroehl, H.W., Rostoker, G., Tsurutani, B.T., Vasyliunas, V.M.: 1994, What is a geomagnetic storm? *J. Geophys. Res.* **99**, 5771. DOI.
- Hajra, R.: 2021a, Variation of the interplanetary shocks in the inner heliosphere. *Astrophys. J.* **917**, 91. DOI.
- Hajra, R.: 2021b, Weakest solar cycle of the space age: A study on solar wind–magnetosphere energy coupling and geomagnetic activity. *Solar Phys.* **296**, 33. DOI.
- Hajra, R.: 2022, Intense, long-duration geomagnetically induced currents (GICs) caused by intense substorm clusters. *Space Weather* **20**, e2021SW002937. DOI.
- Hajra, R., Tsurutani, B.T.: 2018, Interplanetary shocks inducing magnetospheric supersubstorms (SML < -2500 nT): Unusual auroral morphologies and energy flow. *Astrophys. J.* **858**, 123. DOI.
- Hajra, R., Tsurutani, B.T., Echer, E., Gonzalez, W.D., Gjerloev, J.W.: 2016, Supersubstorms (SML < -2500 nT): Magnetic storm and solar cycle dependences. *J. Geophys. Res.* **121**, 7805. DOI.
- Hajra, R., Marques de Souza Franco, A., Echer, E., José Alves Bolzan, M.: 2021, Long-term variations of the geomagnetic activity: A comparison between the strong and weak solar activity cycles and implications for the space climate. *J. Geophys. Res.* **126**, e2020JA028695. DOI.
- Hamilton, D.C., Gloeckler, G., Ipavich, F.M., Stüdemann, W., Wilken, B., Kremser, G.: 1988, Ring current development during the great geomagnetic storm of February 1986. *J. Geophys. Res.* **93**, 14343. DOI.
- Huttunen, K.E.J., Kilpua, S.P., Pulkkinen, A., Viljanen, A., Tanskanen, E.: 2008, Solar wind drivers of large geomagnetically induced currents during the solar cycle 23. *Space Weather* **6**, S10002. DOI.
- Iyemori, T., Takeda, M., Nose, M., Odagi, Y., Toh, H.: 2010, Mid-latitude Geomagnetic Indices ASY and SYM for 2009 (Provisional). <http://wdc.kugi.kyoto-u.ac.jp/aeasy/asy.pdf>.
- Kennel, C.F., Edmiston, J.P., Hada, T.: 1985, *A Quarter Century of Collisionless Shock Research*, Am. Geophys. Union, Washington, 1. ISBN 9781118664032. DOI.
- Klein, L.W., Burlaga, L.F.: 1982, Interplanetary magnetic clouds at 1 AU. *J. Geophys. Res.* **87**, 613. DOI.
- Krieger, A.S., Timothy, A.F., Roelof, E.C.: 1973, A coronal hole and its identification as the source of a high velocity solar wind stream. *Solar Phys.* **29**, 505. DOI.
- Lakhina, G.S., Hajra, R., Tsurutani, B.T.: 2021, In: Gupta, H.K. (ed.) *Geomagnetically Induced Currents*, Springer, Cham, 523. ISBN 978-3-030-58631-7 DOI.
- Loomis, E.: 1861, On the great auroral exhibition of Aug. 28th to Sept. 4th, 1859 and on auroras generally; 8th article. *Am. J. Sci.* **s2-32**, 318. DOI.
- Marques de Souza Franco, A., Hajra, R., Echer, E., Bolzan, M.J.A.: 2021, Seasonal features of geomagnetic activity: A study on the solar activity dependence. *Ann. Geophys.* **39**, 929. DOI.
- Mursula, K., Tanskanen, E., Love, J.J.: 2011, Spring-fall asymmetry of substorm strength, geomagnetic activity and solar wind: Implications for semiannual variation and solar hemispheric asymmetry. *Geophys. Res. Lett.* **38**, L06104. DOI.
- Newell, P.T., Gjerloev, J.W.: 2011, Evaluation of SuperMAG auroral electrojet indices as indicators of substorms and auroral power. *J. Geophys. Res.* **116**, A12211. DOI.

- Oughton, E.J., Skelton, A., Horne, R.B., Thomson, A.W.P., Gaunt, C.T.: 2017, Quantifying the daily economic impact of extreme space weather due to failure in electricity transmission infrastructure. *Space Weather* **15**, 65. [DOI](#).
- Pizzo, V.: 1978, A three-dimensional model of corotating streams in the solar wind, 1. Theoretical foundations. *J. Geophys. Res.* **83**, 5563. [DOI](#).
- Pulkkinen, A., Viljanen, A., Pajunpää, K., Pirjola, R.: 2001, Recordings and occurrence of geomagnetically induced currents in the Finnish natural gas pipeline network. *J. Appl. Geophys.* **48**, 219. [DOI](#).
- Pulkkinen, A., Lindahl, S., Viljanen, A., Pirjola, R.: 2005, Geomagnetic storm of 29–31 October 2003: Geomagnetically induced currents and their relation to problems in the Swedish high-voltage power transmission system. *Space Weather* **3**, S08C03. [DOI](#).
- Schwabe, H.: 1844, Sonnen-Beobachtungen im Jahre 1843. *Astron. Nachr.* **21**, 233.
- Shelley, E.G., Johnson, R.G., Sharp, R.D.: 1972, Satellite observations of energetic heavy ions during a geomagnetic storm. *J. Geophys. Res.* **77**, 6104. [DOI](#).
- Siscoe, G.L.: 1972, Structure and orientations of solar-wind interaction fronts: Pioneer 6. *J. Geophys. Res.* **77**, 27. [DOI](#).
- Smith, E.J., Wolfe, J.H.: 1976, Observations of interaction regions and corotating shocks between one and five AU: Pioneers 10 and 11. *Geophys. Res. Lett.* **3**, 137. [DOI](#).
- Tanskanen, E.I., Pulkkinen, T.I., Viljanen, A., Mursula, K., Partamies, N., Slavin, J.A.: 2011, From space weather toward space climate time scales: Substorm analysis from 1993 to 2008. *J. Geophys. Res.* **116**, A00I34. [DOI](#).
- Temmer, M.: 2021, Space weather: The solar perspective. *Living Rev. Solar Phys.* **18**, 4. [DOI](#).
- Tsurutani, B.T., Gonzalez, W.D.: 1997, *The Interplanetary Causes of Magnetic Storms: A Review*, Am. Geophys. Union, Washington, 77. ISBN 9781118664612. [DOI](#).
- Tsurutani, B.T., Hajra, R.: 2021, The interplanetary and magnetospheric causes of geomagnetically induced currents (GICs) > 10 A in the Mäntsälä Finland pipeline: 1999 through 2019. *J. Space Weather Space Clim.* **11**, 23. [DOI](#).
- Tsurutani, B.T., Gonzalez, W.D., Tang, F., Akasofu, S.I., Smith, E.J.: 1988, Origin of interplanetary southward magnetic fields responsible for major magnetic storms near solar maximum (1978–1979). *J. Geophys. Res.* **93**, 8519. [DOI](#).
- Tsurutani, B.T., Lakhina, G.S., Verkhoglyadova, O.P., Gonzalez, W.D., Echer, E., Guarnieri, F.L.: 2011, A review of interplanetary discontinuities and their geomagnetic effects. *J. Atmos. Solar-Terr. Phys.* **73**, 5. [DOI](#).
- Tsurutani, B.T., Hajra, R., Echer, E., Gjerloev, J.W.: 2015, Extremely intense ($SML \leq -2500$ nT) substorms: Isolated events that are externally triggered? *Ann. Geophys.* **33**, 519. [DOI](#).
- Varley, C.F.: 1873, Discussion of a few papers on Earth currents. *J. Soc. Tel. Eng.* **2**, 111. [DOI](#).
- Viljanen, A., Pirjola, R.: 1989, Statistics on geomagnetically-induced currents in the Finnish 400 kV power system based on recordings of geomagnetic variations. *J. Geomagn. Geoelectr.* **41**, 411. [DOI](#).
- Viljanen, A., Nevanlinna, H., Pajunpää, K., Pulkkinen, A.: 2001, Time derivative of the horizontal geomagnetic field as an activity indicator. *Ann. Geophys.* **19**, 1107. [DOI](#).
- Viljanen, A., Pulkkinen, A., Pirjola, R., Pajunpää, K., Posio, P., Koistinen, A.: 2006, Recordings of geomagnetically induced currents and a nowcasting service of the Finnish natural gas pipeline system. *Space Weather* **4**, S10004. [DOI](#).
- Viljanen, A., Koistinen, A., Pajunpää, K., Pirjola, R., Posio, P., Pulkkinen, A.: 2010, Recordings of geomagnetically induced currents in the Finnish natural gas pipeline – Summary of an 11-year period. *Geophysica* **46**, 59.
- Wang, H., Lühr, H.: 2007, Seasonal-longitudinal variation of substorm occurrence frequency: Evidence for ionospheric control. *Geophys. Res. Lett.* **34**, L07104. [DOI](#).
- Wanliss, J.A., Showalter, K.M.: 2006, High-resolution global storm index: Dst versus SYM-H. *J. Geophys. Res.* **111**, A02202. [DOI](#).
- Williams, D.J.: 1987, Ring current and radiation belts. *Rev. Geophys.* **25**, 570. [DOI](#).